Permeability of asthenospheric mantle and melt extraction rates at mid-ocean ridges

James A. D. Connolly[1], Max W. Schmidt[1], Giulio Solferino[1] & Nikolai Bagdassarov[2]

Magmatic production on Earth is dominated by asthenospheric melts of basaltic composition that have mostly erupted at mid-ocean ridges. The timescale for segregation and transport of these melts, which are ultimately responsible for formation of the Earth's crust, is critically dependent on the permeability of the partly molten asthenospheric mantle, yet this permeability is known mainly from semi-empirical and analogue models[1-6]. Here we use a high-pressure, high-temperature centrifuge, at accelerations of 400g–700g, to measure the rate of basalt melt flow in olivine aggregates with porosities of 5–12 per cent. The resulting permeabilities are consistent with a microscopic model in which melt is completely connected, and are one to two orders of magnitude larger than predicted by current parameterizations[4,7]. Extrapolation of the measurements to conditions characteristic[8] of asthenosphere below mid-ocean ridges yields proportionally higher transport speeds. Application of these results in a model[9] of porous-media channelling instabilities[10] yields melt transport times of ~1–2.5 kyr across the entire asthenosphere, which is sufficient to preserve the observed ^{230}Th excess of mid-ocean-ridge basalts and the mantle signatures of even shorter-lived isotopes such as ^{226}Ra (refs 5,11–14).

The presence of melt in the mantle below mid-ocean ridges (MORs) has been demonstrated using magnetotelluric and seismic reflection sensing[8], the latter suggesting a minimum of 1–2 vol.% melt. Simple flow models that account for mantle flow, the extent of the melting region and the rate of igneous oceanic crust production, place an upper bound on the average sub-MOR melt fraction of 2–4 vol.% (ref. 15). This estimate has been corroborated by melt inclusion studies, which indicate melt fractions of a few per cent in the solid matrix beneath ocean ridges[16,17]. Melt fraction and extraction rates directly control the composition of MOR basalts in terms of strongly incompatible elements and U-series nuclides[7,18]. Particularly at MORs, the preservation of short-lived radiogenic isotopic signatures (of protactinium, radium, thorium and uranium[7]) requires melt flow rates of 10–100 m yr^{-1} or greater if these signatures reflect the onset of melting at depths in excess of 60 km (ref. 8). Such flow rates are too high to be explained by present models for compaction-driven melt expulsion[7,12,13], a discrepancy that has motivated increasingly complex models of melt transport[9,11,19,20]. In this context, permeability is the most uncertain physical parameter controlling the velocity of the melt relative to the solid residuum, that is, the melt segregation velocity and the timescale of melt generation in the mantle.

In this study, we make direct experimental observations of the rate of gravitationally induced flow of basaltic melts through an olivine matrix as a function of matrix porosity. For melts and melt fractions of interest, rates of self-induced compaction-driven flow are insignificant under normal gravitational acceleration in experimental systems. Accordingly, here we use a piston–cylinder device, which permits us to emulate asthenospheric melting conditions, mounted in a centrifuge[21] to enhance melt flow rates.

The experimental charges were mixtures of MOR basalt glass and San Carlos olivine with an average grain size of ~1.8 µm (Methods and Supplementary Table 1) loaded in cylindrical capsules of 2-mm inner diameter. Before centrifuging, the samples were annealed and texturally equilibrated for 24 h in a standard piston–cylinder apparatus at 1,270–1,300 °C and 1.0 GPa (Methods). The annealed samples were loaded into the centrifuging piston–cylinder, whose axis of radial symmetry (the sample axis) is parallel to the centripetal force of the centrifuge. Discounting minor effects due to drag along the capsule walls and the slight shear deformation of the sample on loading, this geometry ensures one-dimensional compaction-driven melt flow along the sample axis as a consequence of centrifuging. Operating conditions for the centrifuge experiments were as follows: g force, 400g–700g; temperature, 1,270–1,300 °C; pressure, 0.9–1.4 GPa; duration, 4–11 h. Melt distributions in the samples were measured from electron backscatter microscopy images of polished sections cut along the sample axis. Each image was divided into five to seven subsections, orthogonal to the sample axis, within which the proportion of melt was determined by image analysis (Fig. 1).

Comparison of the melt distribution in an uncentrifuged sample with the distributions in the centrifuged samples (Fig. 2) demonstrates that centrifuging significantly enhances melt flow and compaction. Neglecting the low solid and melt compressibility, for one-dimensional flow starting from a uniform porosity distribution, the volumetric barycentre of a sample (Fig. 1) is the point at which the porosity is equal to the initial porosity, ϕ_0. Assuming Darcyian flow and a constant pressure gradient at the barycentre, and discounting the effect of grain growth, it follows that the melt velocity relative to the barycentre, $\mathbf{v}_0$, is also constant. Thus

$$\mathbf{v}_0 = \frac{\mathbf{u}_z}{\phi_0 t} \int_0^H (\phi - \phi_0)\, \mathrm{d}z \qquad (1)$$

where ϕ is the melt-filled porosity, t is the duration of the experiment, $\mathbf{u}_z$ is an upward-directed unit vector and H is the z coordinate at the top of the capsule relative to the sample barycentre (that is, half its height). To evaluate the integral in equation (1), the measured porosities were fitted as a linear function of z (Fig. 2), yielding the melt velocities given in Table 1. Upward melt flow is compensated by downward solid flow, that is, compaction of the olivine matrix. Although this process is usually considered to be viscous[2], the observed compaction rates are at least four orders of magnitude greater than those measured experimentally[22] (Methods) for similar materials and physical conditions. These latter rates are consistent with experimental constraints on olivine shear viscosity; thus, we conclude that compaction in our samples was accomplished by a plastic mechanism induced by centrifuging.

[1]Institute for Mineralogy and Petrology, ETH Zurich, 8092 Zurich, Switzerland. [2]Institut für Geowissenschaften, Facheinheit Geophysik, J. W. Goethe Universität, Altenhöferallee 1, 60438 Frankfurt am Main, Germany.
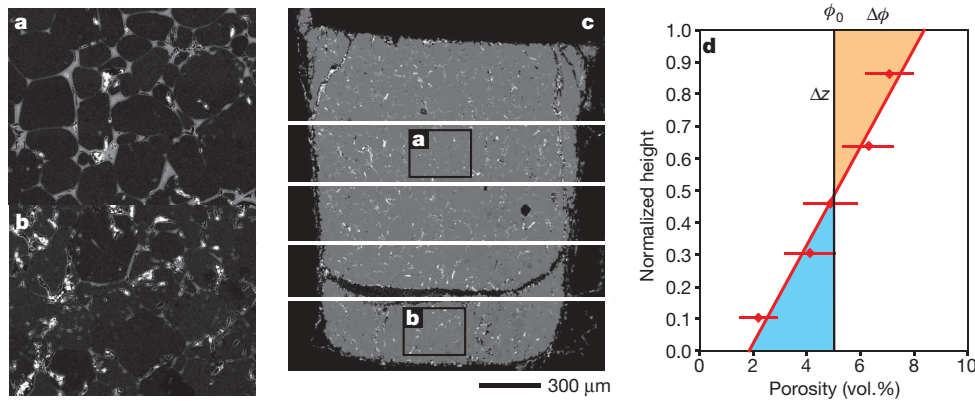
Figure 1 | Centrifuged high-pressure sample and principle of obtaining melt velocities. a–c, Electron backscatter image of an experimental run product: **a** and **b** are details of **c** demonstrating the increase of melt fraction towards the gravitationally defined 'top' of the sample. The grey interstitial phase is melt and the dark granular phase is olivine. The centrifugal acceleration acts downwards. **d,** The average melt content for each slice is fitted as a linear function of height; the intersection with the average porosity defines the barycentre of the sample, at which the porosity corresponds to the average porosity, ϕ_0, and remains constant during the experiment. Error bars, 2σ. The blue and orange areas represent the melt volume that has moved through the barycentre plane, and are used to calculate melt velocities according to equation (1).

Compaction-driven flow of a low-viscosity melt through a creeping matrix has two limiting regimes: a hydraulically limited regime (in which the rate of fluid flow is controlled by the matrix permeability and other hydraulic properties) and a rheologically limited regime (in which the rate of melt flow is controlled by the matrix rheology). To extract the permeability of our samples, we assume melt flow to be hydraulically limited, in which case the hydraulic gradient for melt flow is $\sim -\Delta\rho\mathbf{a}$, where $\Delta\rho$ is the melt–olivine density difference ($\sim 400\ \mathrm{kg\ m}^{-3}$) and $\mathbf{a}$ is the acceleration. According to Darcy's law (Methods), the permeability of the olivine matrix is then

$$k = \frac{\mu|\mathbf{v}_0|\phi_0}{\Delta\rho|\mathbf{a}|} \qquad (2)$$

where μ is the melt viscosity (71 Pa s in the experiments[23]). Applying equation (2) to the experimental results yields permeabilities in the range of $(2\text{–}3) \times 10^{-14}\ \mathrm{m}^2$ for porosities of 5–12% (Table 1). The symmetry of the experimental porosity distributions suggests rheologically rather than hydraulically limited compaction, in which case equation (2) provides a lower bound for the sample permeabilities.
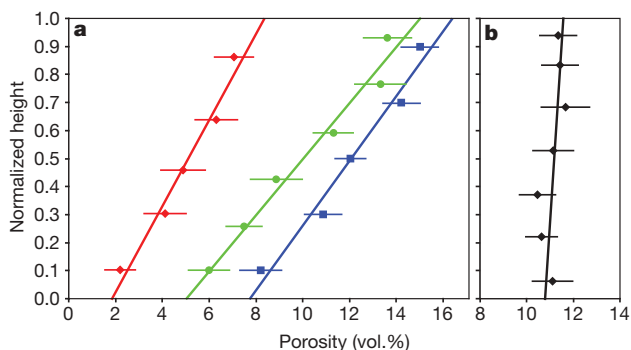

Figure 2 | Profiles of porosity versus sample height for the basaltic melt centrifuged from the olivine matrix. a, The three centrifuged experiments: ZOFB-1 (red), experiment run for 4 h at $700g$ with $\phi_0 = 0.051$; ZOFB-3 (green), 4 h at $600g$ with $\phi_0 = 0.097$; ZOFB-2 (blue), 10.5 h at $400g$ with $\phi_0 = 0.121$. **b,** The static experiment (OFB-5), in which the porosity gradient is not statistically significant. Error bars, 2σ. Although the best fit to the static melt distribution has a slight slope $\mathrm{d}\phi/\mathrm{d}z$, a vertically homogeneous melt distribution can be fitted within the errors. The integral of equation (1) is thus formulated with ϕ_0 as the reference melt distribution along the sample axis. We note that the static experiment also had an annealing time three times longer than in ZOFB-3, the longest-centrifuged experiment, allowing for much longer thermal melt migration.

Models of asthenospheric melt flow generally presume that permeability can be expressed as a function of porosity and grain size within the solid aggregate[2]:

$$k = \frac{d^2\phi^n}{C} \qquad (3)$$

where d is grain size and C and n are parameters that depend on the geometry of the microscopic hydraulic bonds. A quadratic porosity dependence in equation (3) (that is, $n = 2$) is appropriate when melt first exceeds the percolation threshold and becomes interconnected along grain edges[3,5]. At the higher porosities of our experiments (Fig. 1), this dependence becomes cubic[4–7] ($n = 3$) and estimates for the constant C range from 50 to 1,000 (ref. 2), with more recent estimates converging towards values of 200–300 (refs 4,5,7). In contrast, our observations yield C values in the range of 3–27, suggesting that for a given porosity, permeabilities are up to two orders of magnitude greater than previously supposed. Within measurement error, our values for C are constant, but the error does not account for the possibility that the hydraulic gradient during rheologically limited compaction may be much less than $\Delta\rho\mathbf{a}$.

Reference [22] reports an experimental study of forced compaction-driven flow of lithium silicate, basaltic and albitic melts through an olivine matrix. Although we suggest that the experimental results of ref. 22 do not constrain the matrix permeability with respect to the basaltic and lithium silicate melts (Supplementary Information), the experiment on albite places an upper bound on C in the range of 4–17, in agreement with our results.

The experimental results are also confirmed by a microscopic geometric model[24,25] that yields $C = 135\pi^2/64 \approx 20$ if it is assumed that hydraulic conductivity is limited by flow along the faces of cubic solid grains. The transition between cubic and quadratic porosity dependence is dependent on the microscopic melt distribution and, therefore, on chemistry[3], but for the anhydrous olivine/basalt system full connectivity is achieved for porosities of 2–3%. This is reported in ref. 5, which posits that the variation in the nature of the microscopic hydraulic bonds with porosity may lead to a large increase in permeability when full connectivity is achieved. The relatively high porosities of our experiments preclude observation of this transition, but as the grain boundaries in our experiments are saturated in melt, we conclude that C is unlikely to be much lower than the value inferred from our experiments.

Taken at face value, our preferred value of $C = 10$ results in sub-MOR melt transport speeds of 2–150 m yr^{-1} for uniform flow, assuming plausible upper-asthenospheric parameters ($d = 10^{-2}$ m (ref. 26), $\mu = 10$ Pa s, $\Delta\rho = 500\ \mathrm{kg\ m}^{-3}$) and porosities of $10^{-2 \pm 0.5}$, as indicated by sub-MOR geophysical observations[8].

Table 1 | Experimental conditions, calculated melt segregation velocities and permeabilities

Run	T (°C)	P (GPa)	$\|\mathbf{a}\|/g$	t_{static} (min)	$t_{centrif}$ (min)	ϕ_0	$\dot{\phi}$ (s^{-1})	$\|\mathbf{v_0}\|$ (m s^{-1})	k (m^2)	d (μm)	C
OFB-5	1,285	1.0	1	4,320	—	0.112(9)	—	—	—	32.9(10)	—
ZOFB-1	1,270	1.4	700	1,320	273	0.051(9)	3.9×10^{-5}	$1.4(6) \times 10^{-8}$	$2.0(1.1) \times 10^{-14}$	22.2(11)	3.2(1.9)
ZOFB-3	1,285	0.9	600	1,440	251	0.097(8)	3.3×10^{-5}	$1.1(3) \times 10^{-8}$	$2.9(1.2) \times 10^{-14}$	21.0(8)	13.6(5.6)
ZOFB-2	1,300	1.3	400	1,260	627	0.121(7)	9.4×10^{-5}	$3.3(9) \times 10^{-9}$	$2.0(0.8) \times 10^{-14}$	17.7(8)	27(12)

Here T and P are respectively the experimental pressures and temperatures, $|\mathbf{a}|/g$ is the centrifugal acceleration divided by the acceleration due to gravity at the Earth's surface, t_{static} and $t_{centrif}$ are respectively the annealing and centrifuging times, ϕ_0 is the average melt fraction or porosity, $\dot{\phi}$ is the maximum time-averaged compaction rate (Methods; approximated by $\Delta\phi/t\phi_0$), $\mathbf{v_0}$ is the melt velocity (equation (1)), k is the permeability (equation (2)), d is the time-integrated average grain size during centrifugation (assuming that grain growth is proportional to log d/log t; this correction amounts to ~ −5% of the measured grain size at the end of the experiments), and C is the constant in the permeability–porosity relationship (equation (3)).

MOR basalt U-series isotopic excesses are an important indirect source of information about the details of sub-ridge melt flow. Excesses in the long-lived isotopes ^{230}Th (half-life, $t_{1/2} = 75,000$ yr) and ^{231}Pa ($t_{1/2} = 32,800$ yr) can be generated by minute degrees of partial melting (<0.1%) in volatile-rich heterogeneities at the base of the melting region at depths of 60–120 km (ref. 27). However, three possibilities are debated for the origin of excesses in more short-lived isotopes, notably ^{226}Ra ($t_{1/2} = 1,600$ yr). One hypothesis assumes that the more voluminous melting at depths of <60 km, which produces geophysically observable melt fractions of order 10^{-2}, do not fractionate U-series elements. Consequently, all excesses have a common origin in the lower part of the melting column. Transport times from the bottom of the melting column to the MOR are then constrained by the ^{226}Ra half-life[12–14], the observed magnitude of ^{226}Ra excesses suggesting transport in less than twice the ^{226}Ra half-life. An alternative explanation draws on the observation that the sub-MOR melt flow is strongly channelized[10,28] and proposes that MOR basalt ^{226}Ra excess is generated by admixture of shallow interchannel partial melts, thereby circumventing the problem of transporting the ^{226}Ra excess from depths of 120 km (refs 29,30). A third hypothesis explores the generation of excess ^{226}Ra through diffusive exchanges between melt and minerals in both the asthenospheric melt column and the lithosphere[31]. Our measurements have little bearing on the contribution of these exchange processes to the observed ^{226}Ra excesses; but because permeability is closely related to transport speed, our measurements constrain the feasibility of a common deep origin for MOR basalt U-series isotopic excesses.

There is consensus that some degree of channelization is necessary to preserve lower-asthenospheric isotopic signatures[30]. Evidence from exhumed asthenospheric rocks[28,32] suggests that this channelization occurs as a consequence of porous-media flow instabilities. Models proposed to explain such instabilities include reactive transport[10,19], shear-enhanced segregation[20] and rheologically induced mechanical instability[9]. We consider the third of these (Methods) because the instability growth rate can be expressed analytically and is independent of external forcings. By this mechanism[9], a domain of anomalous melting initiates a channelling instability. To a first approximation, the growth rate and speed of the instability are respectively proportional to $C^{0.5}$ and C^{-1}. The onset of melting would be characterized by low melt viscosities, of 0.1–0.5 Pa s, and background melt fractions of $\phi_0 \approx 10^{-3}$. Taking $C = 10$, as suggested by our analysis, an instability with an initial amplitude of $5\phi_0$ would rise through the lower 60 km of the asthenosphere in 400–1,800 yr, increasing its melt volume about twofold (Fig. 3a). In contrast, for $C = 250$, a value from the previously accepted range for C, melt volumes increase three- to five-fold but transport times from depths of 120 to 60 km become 8,000–34,000 yr.

Assuming that such instabilities survive the transition from the lower to the upper asthenosphere, where melt production is more homogeneous, the resulting melts are more viscous ($\mu \approx 10$ Pa s) and background melt fractions are of the order of $\phi_0 \approx 10^{-2}$ (ref. 8), transport times are ~700 yr for $C = 10$, as opposed to ~10,000 yr for $C = 250$ (Fig. 3b). Our results thus show that porous-media channelling instabilities are able to transfer melt from the bottom of the melting column to the MOR in 1,000–2,500 yr, which is fast enough to allow ^{226}Ra excesses to originate from the bottom of the melting column. Because the velocity scale for compaction-driven

melt transport is directly proportional to the permeability constant, C (ref. 2), we expect that our results also imply an order-of-magnitude decrease in transport timescales inferred for reactive transport[10] and shear-induced melt segregation[20].
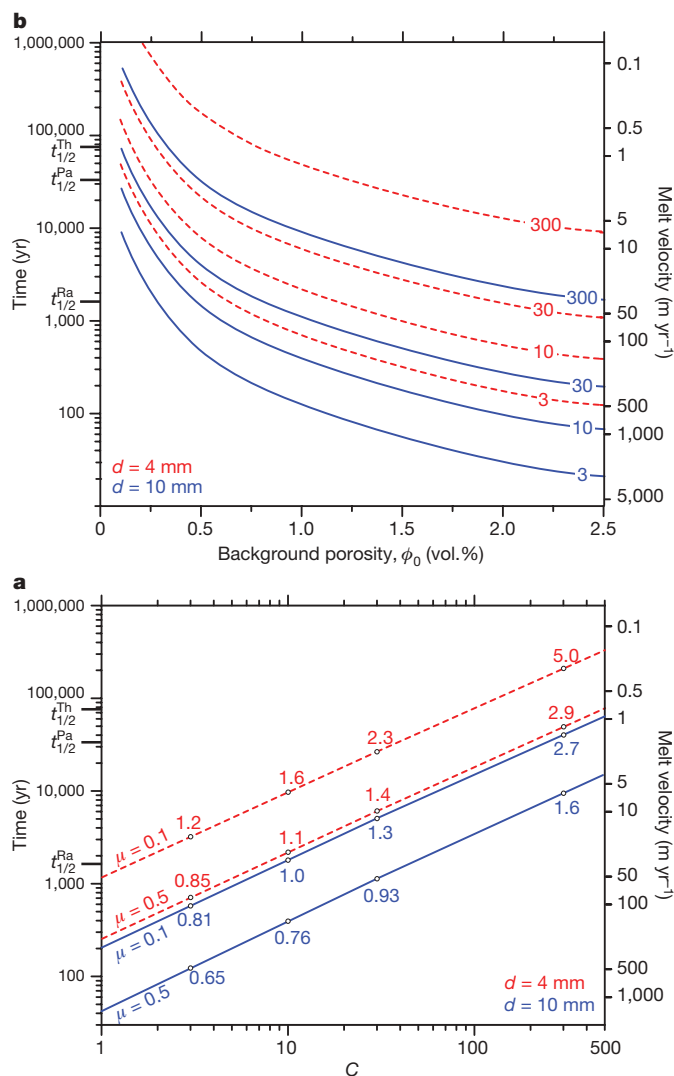

Figure 3 | Transport times and melt speeds below MORs. a, Time for a melt channelling instability to traverse the lower MOR asthenosphere (depth, 120–60 km), with background porosity $\phi_0 = 10^{-3}$, as a function of the permeability constant, C, grain size, d, and melt viscosity, μ. The numbers on individual points give resulting porosities within the instability (in vol.%) at a depth of 60 km. **b,** Time for a melt channelling instability to traverse the upper MOR asthenosphere (depth, 60–0 km) as a function of background porosity, ϕ_0, grain size, d, and the permeability constant, C (labelling the lines). Our preferred value is $C = 10$. The half-lives of ^{226}Ra, ^{231}Pa and ^{230}Th are $t_{1/2}^{Ra}$, $t_{1/2}^{Pa}$ and $t_{1/2}^{Th}$, respectively. In all cases, the instability nucleates from a perturbation with amplitude $5\phi_0$, the solid viscosity is 10^{19} Pa s, the difference between the solid and the melt density is 500 kg m^{-3}, and the upper-asthenospheric melt viscosity is 10 Pa s. The calculation of transport times is discussed in Methods.

METHODS SUMMARY

Starting materials were a mixture of natural San Carlos olivine and synthetic MOR basalt glass with a magnesium number (Mg# = 100Mg/(Mg+Fe)) of 0.80 (Supplementary Table 1). Olivine powder with an average grain size of ~1.8 μm, measured by laser diffractometry of dispersed solutions, was obtained by crushing and milling. The MOR basalt glass was made from natural and synthetic oxide powders in a platinum crucible at 1,300 °C with an oxygen fugacity (f_{O_2}) such that $\log f_{O_2} = -6.704$ (equivalent to quartz–fayalite–magnetite at 1,300 °C and 1 GPa).

Experiments for annealing were performed in an end-loaded, 14-mm-bore piston–cylinder, using double platinum–graphite capsules. The bore sizes and salt/pyrex/graphite/crushable MgO assemblies of the static and centrifuging piston–cylinder devices were identical[21], the graphite furnaces were 6.0 mm in inner diameter and 36 mm in length, and the platinum capsules were 4 mm in outer diameter and typically 7 mm in length. The capsules were placed such that the hot spot was centred on the sample. Temperature was controlled to a precision of ±5 °C and the temperature gradient along the length of the capsule was <10 °C. The arrangement in the centrifuging piston–cylinder was such that the assembly axis was radial, with the thermocouple towards the centre, the bottom of the capsule facing the thermocouple and acceleration directed along the axis of the capsule towards its lid.

Melt distribution. Polished sections of the run products were imaged using backscattered electrons and olivines were analysed by wavelength-dispersive spectrometry using a Jeol JXA-8200 microprobe. Melt pools were too small to analyse. Melt abundances along the capsule and average grain sizes of olivines were obtained through digital analysis of backscattered-electron images using the software IMAGETOOL version 3.0 (The University of Texas Health Science Center; http://ddsdx.uthscsa.edu/dig/itdesc.html).

Full Methods and any associated references are available in the online version of the paper at www.nature.com/nature.

1. Maaloe, S. & Scheie, A. The permeability controlled accumulation of primary magma. *Contrib. Mineral. Petrol.* **81,** 350–357 (1982).
2. McKenzie, D. The generation and compaction of partially molten rock. *J. Petrol.* **25,** 713–765 (1984).
3. Van Bargen, N. & Waff, H. S. Permeabilities, interfacial areas and curvatures of partially molten systems: results of numerical computations of equilibrium microstructures. *J. Geophys. Res.* **91,** 9261–9276 (1986).
4. Wark, D. A., Williams, C. A., Watson, E. B. & Price, J. D. Reassessment of pore shapes in microstructurally equilibrated rocks, with implications for permeability of the upper mantle. *J. Geophys. Res.* **108,** doi:10.1029/2001JB001575 (2003).
5. Faul, U. H. Melt retention and segregation beneath mid-ocean ridges. *Nature* **410,** 920–923 (2001).
6. Cheadle, M. J., Elliott, M. T. & McKenzie, D. Percolation threshold and permeability of crystallizing igneous rocks: the importance of textural equilibrium. *Geology* **32,** 757–760 (2004).
7. Richardson, C. & McKenzie, D. Radioactive disequilibria from 2D models of melt generation by plumes and ridges. *Earth Planet. Sci. Lett.* **128,** 425–437 (1994).
8. The MELT Seismic Team. Imaging the deep seismic structure beneath a mid-ocean ridge: the MELT experiment. *Science* **280,** 1215–1218 (1998).
9. Connolly, J. A. D. & Podladchikov, Y. Y. Decompaction weakening and channeling instability in ductile porous media: implications for asthenospheric melt segregation. *J. Geophys. Res.* **112,** doi:10.1029/2005JB004213 (2007).
10. Kelemen, P. B., Hirth, G., Shimizu, N., Spiegelman, M. & Dick, H. J. B. A review of melt migration processes in the adiabatically upwelling mantle beneath oceanic spreading ridges. *Phil. Trans. R. Soc. Lond. A* **355,** 283–318 (1997).
11. Spiegelman, M., Kelemen, P. B. & Aharonov, E. Causes and consequences of flow organization during melt transport: the reaction infiltration instability in compactible media. *J. Geophys. Res.* **106,** 2061–2077 (2001).
12. McKenzie, D. Constraints on melt generation and transport from U-series activity ratios. *Chem. Geol.* **162,** 81–94 (2000).
13. Rubin, K. H., van der Zander, I., Smith, M. C. & Bergmanis, E. C. Minimum speed limit for ocean ridge magmatism from ^{210}Pb–^{226}Ra–^{230}Th disequilibria. *Nature* **437,** 534–538 (2005).
14. Stracke, A., Bourdon, B. & McKenzie, D. Melt extraction in the Earth's mantle: constraints from U–Th–Pa–Ra studies in oceanic basalts. *Earth Planet. Sci. Lett.* **244,** 97–112 (2006).
15. Spiegelman, M. & McKenzie, D. Simple 2-D models for melt extraction at mid-ocean ridges and island arcs. *Earth Planet. Sci. Lett.* **83,** 136–152 (1987).
16. Johnson, K. T. M., Dick, H. J. B. & Shimizu, N. Melting in the oceanic upper mantle: an ion microprobe study of diopsides in abyssal peridotites. *J. Geophys. Res.* **95,** 2661–2678 (1990).
17. Sobolev, A. V. & Shimizu, N. Ultra-depleted primary melt included in an olivine from the Mid-Atlantic Ridge. *Nature* **363,** 151–154 (1999).
18. Salters, V. J. M. & Longhi, J. Trace element partitioning during the initial stages of melting beneath mid-ocean ridges. *Earth Planet. Sci. Lett.* **166,** 15–30 (1999).
19. Daines, M. J. & Kohlstedt, D. L. The transition from porous to channelized flow due to melt/rock reaction during melt migration. *Geophys. Res. Lett.* **21,** 145–148 (1994).
20. Holtzman, B. K. Groebner, N. J., Zimmermann, M. E., Ginsberg, S. B. & Kohlstedt, D. L. Stress-driven melt segregation in partially molten rocks. *Geochem. Geophys. Geosyst.* **4,** doi:10.1029/2001GC000258 (2003).
21. Schmidt, M. W., Connolly, J. A. D., Günter, D. & Bogaerts, M. Element partitioning: the role of melt structure and composition. *Science* **312,** 1646–1650 (2006).
22. Renner, J. Viskupic, K. Hirth, G. & Evans, B. Melt extraction from partially molten peridotites. *Geochem. Geophys. Geosyst.* **4,** doi:10.1029/2002GC000369 (2003).
23. Bottinga, Y. & Weill, D. F. The viscosity of magmatic silicate liquids: a model for calculation. *Am. J. Sci.* **272,** 438–475 (1972).
24. Dienes, J. K. in *Issues in Rock Mechanics* (eds Goodman, R. E. & Heuze, F. E.) 86–94 (American Institute of Mining, Metallurgical, and Petroleum Engineers, 1982).
25. Connolly, J. A. D., Holness, M. B., Rubie, D. C. & Rushmer, T. Reaction-induced microcracking: an experimental investigation of a mechanism for enhancing anatectic melt extraction. *Geology* **25,** 591–594 (1997).
26. Mercier, J. C. Magnitude of the continental lithospheric stresses inferred from rheomorphic petrology. *J. Geophys. Res.* **85,** 6293–6303 (1980).
27. Hirth, G. & Kohlstedt, D. L. Water in the oceanic upper mantle: implications for rheology, melt extraction and the evolution of the lithosphere. *Earth Planet. Sci. Lett.* **144,** 93–108 (1996).
28. Kelemen, P. B., Shimizu, N. & Salters, V. J. M. Extraction of mid-ocean-ridge basalt from the upwelling mantle by focused flow of melt in dunite channels. *Nature* **375,** 747–753 (1995).
29. Spiegelman, M. & Elliott, T. Consequences of melt transport for uranium series disequilibrium in young lavas. *Earth Planet. Sci. Lett.* **118,** 1–20 (1993).
30. Lundstrom, C. C. Uranium-series disequilibria in mid-ocean ridge basalts: observations and models of basalt genesis. *Rev. Mineral. Geochem.* **52,** 175–214 (2003).
31. Van Orman, J. A., Saal, A. E., Bourdon, B. & Hauri, E. H. Diffusive fractionation of U-series radionuclides during mantle melting and shallow-level melt-cumulate interaction. *Geochim. Cosmochim. Acta* **70,** 4797–4812 (2006).
32. Bouilhol, P. *et al.* Recording of arc crust-mantle transition zone formation by melt-rock reaction: evidence from ultramafic rocks of Sapat (Kohistan, Northern Pakistan). *Lithos* **107,** 17–37 (2009).

METHODS

Fluid velocity relative to the sample barycentre. Equation (1) is obtained by integrating the conservation equation for melt mass

$$\frac{\partial \phi}{\partial t} + \nabla \bullet (\phi \mathbf{v}) = 0 \tag{4}$$

over time and space. Equation (1) is the melt velocity relative to the barycentre rather than the true Darcyian velocity, $\mathbf{v}$, which is measured relative to the solid matrix. However, for one-dimensional compaction involving incompressible phases, conservation of total mass relates the solid and fluid velocities at the volumetric barycentre as follows:

$$(1 - \phi_0)\mathbf{v}_{0,s} + \mathbf{v}_0 \phi_0 = 0 \tag{5}$$

where $\mathbf{v}_{0,s}$ is the barycentric solid velocity. Thus, assuming the maximum possible hydraulic gradient of $-(1 - \phi)\Delta\rho\mathbf{a}$ for a self-compacting system, Darcy's law is

$$(\mathbf{v}_0 - \mathbf{v}_{0,s})\phi_0 = \frac{k}{\mu}(1 - \phi_0)\Delta\rho\mathbf{a} \tag{6}$$

By making use of equation (5) to express the barycentric solid velocity as a function of $\mathbf{v}_0$ and ϕ_0, equation (6) can be simplified to equation (2).

Rheologically limited compaction rate. When the matrix has a much greater viscosity than its interstitial fluid, the viscous compaction rate[33,34] is

$$\dot{\phi} = \frac{1}{\phi}\frac{\mathrm{d}\phi}{\mathrm{d}t} = -\frac{3}{4}\frac{p_e}{\eta} \tag{7}$$

where p_e is the effective pressure and η is the shear viscosity of the solid grains. We compute the olivine shear viscosity from the constitutive relation

$$\eta = \frac{d^3}{3A}\exp\left(\frac{E + pV}{RT}\right) \tag{8}$$

for diffusion creep in dry olivine as constrained experimentally[35], where p is pressure (in pascals), T is temperature (in kelvin), R is the molar gas constant, d is grain size (in metres), $E = 375 \times 10^3\,\mathrm{J\,mol^{-1}}$, $V = 6 \times 10^{-6}\,\mathrm{m^3}$ and $A = 1.5 \times 10^{-15}\,\mathrm{m^3\,Pa^{-1}\,s^{-1}}$. For rheologically limited compaction[34], the effective pressure is

$$p_e = -\int (1 - \phi)\Delta\rho|\mathbf{a}|\ \mathrm{d}z \approx -\Delta\rho|\mathbf{a}|z$$

and attains its greatest magnitude at the top and bottom of the sample, $z = \pm H$. The observed compaction rates (Table 1) are 10^5 (ZOFB-3) to 10^6 (ZOFB-1) times faster than those predicted from equations (7) and (8). Although dry olivine is not necessarily an appropriate model for compaction of a melt-saturated matrix; the compaction rates reported in ref. 22 for olivine plus basalt melt are in good agreement with those computed from equations (7) and (8), with steady-state compaction rates being less than two orders of magnitude greater than predicted. This suggests that although viscous creep plausibly explains the observations in ref. 22, compaction must have been accelerated in our experiments by a plastic mechanism activated by centrifuging.

Mechanical channelling instability. To quantify the properties of buoyancy-induced channelling instabilities that result from compaction-driven fluid flow through a viscous matrix that weakens under high fluid pressure, we follow ref. 9 in characterizing the weakening by a reduced viscosity during decompaction. For this case, numerical modelling[9] has demonstrated that in porous media with a cubic porosity–permeability relationship, a domain of anomalous melting initiates an instability that grows such that the amplitude of the instability measured relative to the background melt fraction, ϕ_0, at time t is

$$\alpha \approx \alpha_0 + \frac{t}{\kappa^{3/8}}\sqrt{\frac{C\mu}{d^2\phi_0^2\eta}} \tag{9}$$

where α is the amplitude of the instability measured relative to the background melt fraction, ϕ_0, at time t, and we set $\eta = 10^{19}\,\mathrm{Pa\,s}$ and $d = 0.01\,\mathrm{m}$. The parameter κ characterizes weakening during decompaction. A value of $\kappa < 10^{-2}$–10^{-3} is necessary to reproduce channelization patterns inferred from natural systems[10,32]; accordingly, we take $\kappa = 10^{-3}$. The speed of the instability is

$$c = \frac{d^2\phi_0^2\Delta\rho g}{C\mu}\frac{1 + (3\ln\alpha - 1)\alpha^3}{1 + (\alpha^2 - 3)\alpha/2}$$

The time required for an instability of initial amplitude α_0 to propagate a distance δz is therefore obtained by solving the transcendental equation

$$\delta z - \int c\ \mathrm{d}t = 0 \tag{10}$$

This analysis presumes that the porosity distribution generated by anomalous melting is close to that of the quasi-steady-state solution observed numerically. When this assumption is invalid, the time required for the porosity distribution to evolve towards a quasi-steady state is of the order of the compaction timescale. As the instability grows by draining melt from the background porosity, short-lived radiogenic isotope excesses (for example for ^{226}Ra) can be generated after nucleation. The volume of melt transported is approximately linearly proportional to the instability amplitude.

Whether such instabilities would persist in the upper asthenosphere, where melt production is homogeneous, the melts are more viscous and background melt fractions are $\sim 10^{-2}$, remains to be demonstrated. However, assuming that the instabilities survive the transition, the initial amplitude of the instability in the upper regime would be

$$\alpha'_0 \approx \alpha\left(\frac{\phi_0}{\phi'_0}\right)^4\left(\frac{\mu'}{\mu}\right)^{3/2} \tag{11}$$

where primes denote upper asthenospheric properties.

33. Wilkinson, D. S. & Ashby, M. F. Pressure sintering by power law creep. *Acta Metall.* **23**, 1277–1285 (1975).
34. Connolly, J. A. D. & Podladchikov, Y. Y. Temperature-dependent viscoelastic compaction and compartmentalization in sedimentary basins. *Tectonophysics* **324**, 137–168 (2000).
35. Hirth, G. & Kohlstedt, D. L. in *Inside the Subduction Factory* (ed. Eiler, J. M.) 83–106 (Geophys. Monogr. 138, American Geophysical Union, 2003).